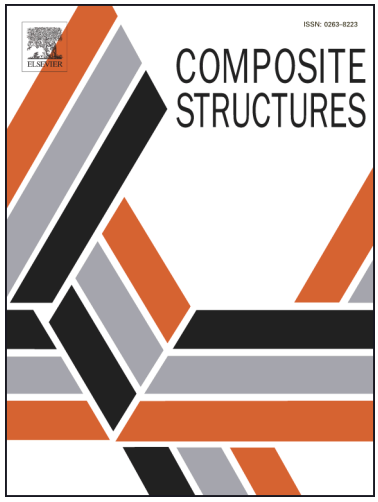

Uniaxial Compression Mechanical Properties and Fracture Characteristics of Brucite Fiber Reinforced Cement-Based Composites

Yuanyi Yang, Yi Deng, Xingkui Li

PII: S0263-8223(18)30983-8
DOI: https://doi.org/10.1016/j.compstruct.2019.01.030
Reference: COST 10547

To appear in: *Composite Structures*

Received Date: 12 March 2018
Revised Date: 20 December 2018
Accepted Date: 3 January 2019

Please cite this article as: Yang, Y., Deng, Y., Li, X., Uniaxial Compression Mechanical Properties and Fracture Characteristics of Brucite Fiber Reinforced Cement-Based Composites, *Composite Structures* (2019), doi: https://doi.org/10.1016/j.compstruct.2019.01.030

Uniaxial Compression Mechanical Properties and Fracture Characteristics of Brucite Fiber Reinforced Cement-Based Composites

Yuanyi Yang[a,b], Yi Deng[c,d,*], Xingkui Li[b]

[a] College of Materials and Chemistry & Chemical Engineering, Chengdu University of Technology, Chengdu 610065, China

[b] Department of Materials Engineering, Sichuan College of Architectural Technology, Deyang 618000, China

[c] School of Chemical Engineering, Sichuan University, Chengdu 610065, China

[d] Department of Mechanical Engineering, The University of Hong Kong, Hong Kong, 999077, China

*Corresponding author:

A/Prof. Yi Deng,

School of Chemical Engineering, Sichuan University,

Department of Mechanical Engineering, The University of Hong Kong,

E-mail: dengyibandeng@scu.edu.cn; dengyi@hku.hk.

Abstract: In this work, the mechanical properties, stress-strain behaviors, and microstructure of brucite fiber reinforced cement-based composites are determined. The results reveal that the incorporation of brucite fiber limits the compressive strength reinforcement of cement-based composite but leads to a significant increase of tensile strength by 136% and flexural strength by 73%. The employment of brucite

fiber increases the fracture toughness K_{Ic}^{S} and K_{Ic}^{Q} of the cement-based composite by 450% and 98%. The incorporation of brucite fiber increases the linear elastic fracture toughness energy G_F by 455% and elastic-plastic fracture toughness energy J_C by 279%. The constitutive model of brucite fiber reinforced cement paste is also established. The diameter of the brucite fiber bundle is 1.5-16.3μm, and the diameter of the single dispersed fiber is around 45-110nm. There are about 15-363 single fibers in a bundle. Due to the brucite fiber possesses an intrinsic fibrous anisotropy, and network topology, the brucite fiber reinforced cement composites exhibit advantages of greater bending strength and crack bridging, as well as better crack resistance properties.

Keywords: Uniaxial compression, Fracture toughness, Cement composite, Brucite fiber.

1. Introduction

Development of construction project applications causes an urgent need to explore higher performance construction materials possessing high strength, toughness, cracking resistance, durability, etc. Fiber reinforced cement composite (*FRCC*) is one of the engineering materials, which are extensively used to enhance the structural resistance and performance under various loading combinations. However, ordinary *FRCC* is costly, and the production of *FRCC* increases the energy consumption and carbon footprint, one possible solution is to employ eco-friendly and economic fibers in *FRCC* to address the question. Brucite fiber is a kind of naturally existing fibrous mineral which is formed in an alkaline medium [1]. The main chemical composition of brucite is $Mg(OH)_2$, and the crystal structure of brucite fiber belongs to the trigonal crystal system and octahedron structure. The length of brucite fiber used as an additive to reinforce cement or asphalt is generally 10-80 mm [3]. Compared with other fibers such as polyester fiber, basalt fiber, and glass fiber, brucite fiber possesses excellent properties including fiber bundle-splitting, dispersing properties and compatible with the silicate cement [6, 7, 10]. Brucite fiber is also quite different from asbestos in chemical compositions, crystal structures, and chemical properties, and it has been proved that brucite fiber is a harmless mineral to the human body [3-5]. With excellent anti-alkaline property (brucite fiber exists stably in strongly alkaline medium with an alkaline loss of 2%), good mechanical performance (tensile strength is around 900 MPa) [6], reasonable price and abundant resources [5], the employment of brucite fiber is dependable and environmental in the industrial applications.

The study on brucite fiber used in cement was firstly conducted by Kaiping Liu et al. in 2004. Their study demonstrated the potential of brucite fiber in reinforced cement [7]. Bowen Gua et al. has reported that brucite fiber exerted its high tensile strength on concrete, and the mechanical property of the fibrous cement matrix with the improvement of the dispersing action of water reducers [8]. Rui Xiong et al. has investigated the fatigue property of brucite fiber asphalt mixture under the action of sulfate erosion. The results showed that brucite fiber effectively improved the fatigue property of the asphalt mixture in sulfate corrosion environment [9]. Bowen Guan et al. found that brucite fiber had good preservation in the moist storage environment. Asphalt mixture prepared with brucite fiber also has excellent high-temperature stability, water sensitivity, and fatigue property, especially low-temperature properties [10, 11]. Xingkui Li [12] previously investigated the dispersion and performance of brucite fibers in the cement slurry. The results show that the micro-crack initiation and propagation in cement pasted was restricted by brucite fiber, and the tensile strength increased significantly. Ming Li et al. [13] has studied the tri-axial stress-strain tests of brucite fiber reinforced well-cementing stones, and they found that the application of brucite fiber-containing cement slurries displayed satisfactory mechanical performances, and the elasticity modulus of well-cementing stones was reduced obviously. Form above, previous works are concentrated on the strength enhancement, durability, and workability of brucite fiber reinforced cement-based composite, but no comprehensive studies have been conducted on the constitutive relation, macroscopic constitutive model and fracture toughness of brucite fiber reinforced cement-based

composite, which are keys to the comprehensive capabilities of the brucite fiber reinforced cement-based composite. Hence, this work can provide the structure guidance and design of elements subjected to axial force.

This work has presented an investigation on the uniaxial compression, and fracture toughness of brucite fiber reinforced cement composite. It aims to comprehend further the physical properties of *FRCC*. The strengthening, anti-crack and toughening mechanism of the brucite fiber in cement composite are also discussed, which are helpful for further research and application on the *FRCC*. Moreover, the experiment results are also useful in the development of quantization for toughening behavior in fiber reinforced cement elements.

2. Materials and Methods

2.1. Raw materials

The raw materials used in this manuscript include cement (G high sulfur resistant oil-well cement, Sichuan, China), brucite fiber (Shijiazhuang, Hebei province, China), water reducer (phenol and formaldehyde condensation polymer, Chengdu, China), de-foaming agent (dibutyl phosphate, Chengdu, China) and tap water. The basic properties and chemical constituents of brucite fiber were shown in Table S1.

2.2. Experimental techniques

2.2.1. Pastes preparation

The cement slurry incorporated brucite fiber was produced based on the Chinese standard “GB 10238-2005 Oil-well Cement” and “GB/T 19139-2012: The application performance and test methods of oil-well cement”.

The mixing procedures were illustrated in Fig. S1. The brucite fiber was mixed with the cement powder for 5 min as pre-dispersion. Afterward, the curing condition of the cement slurry was under the relative humidity 95% and 30 ℃ for 7 days as preparation.

2.2.2. Test methods

The split tensile strength of the cement pastes was a test based on the Chinese standard “GB/T 50081-2002: The standard of concrete mechanics performance test method”. The test specimen size of the cement pastes was molded as 70.7 mm×70.7 mm×70.7 mm.

The uniaxial compression experiment of cement pastes was tested by a CMT-300 universal testing machine (300 kN maximum test load, 0.5 accuracy index, Shandong Jinan Lian engineering testing technology Co., Ltd.). The test specimen size of the cement pastes for uniaxial compression experiment was 70.7 mm×70.7 mm×70.7 mm as well. The displacement control mode with a loading rate of 0.06mm/s was used in this experiment. Additionally, the test data was collected by the computer software.

The fracture toughness experiment of cement pastes was tested by three-point bending test according to the ASTM C34, ASTM C1609, and Chinese standard CECS13. The CMT-300 universal testing machine was also used to determine the strength and toughness, and the test fixture was presented in Fig. S2. The specimen

size employed in this test was 40×40×160 mm. The initial notch depth was 12 mm at midspan of the specimen. The span of welding pedestals was 100 mm, and the loading rate was set to 0.02 mm/min.

Fracture surfaces and microstructure of the specimens were examined using a scanning electron microscopy (JSM-6490LV, Company of JEOL, Japan).

In this manuscript, specimens were prepared according to the proportions in Table 1. Besides, the cement additives and the brucite fiber used in this manuscript were mixed with the cement powder according to the quality fraction of the cement.

3. Results and discussion

3.1. Strength properties

Two different types of brucite fibers (as shown in Table S1) were employed in this manuscript. A comparison of the cement pastes incorporated two different brucite fibers was made to determine the influence of the brucite fiber amount on physical performance and to figure out the optimum dosage. Fig. 1(a, b) showed that although the strengthening effect of brucite fiber was observed, the mechanical strength fluctuated with the increasing of the brucite fiber. The optimum dosage of type *A* was 5% for the best physical performance, and the optimum dosage of type *B* was 1%. Moreover, at a relatively high amount, the incorporation of brucite fiber in the cement pastes seriously influenced the fiber distribution and slurry flowability, which leads to a decrease in matrix strength. The increasing ratios of the different amount of brucite fiber reinforced cement pastes were presented in Table S2. Caused by the relative low

Young's modulus of brucite fiber compared to cement stone, the incorporation of brucite fiber limited the reinforcement of compressive strength, whereas there was an improvement on the tensile strength and deformability of cement pastes. It is in accordance with the test results of brucite-fiber-reinforced cement mortar from prior works [14-18]. The increasing ratio of the splitting tensile strength to the compression strength indicated that incorporating any type of brucite fibers can increase the durability of the cement-based material. Since the strength data so discrete that cannot elucidate the toughness sufficiently, a further analysis in-depth was needed to quantify and evaluate the effect of brucite fiber employed in cement-based material, and the type A brucite fiber was selected for further exploration in the following parts.

3.2. Stress-strain curve

3.2.1. Stress-strain responses under uniaxial compression

From the prior works [17], the appearance of plastic deformation, micro-crack initiating and propagation, peak strength as well as the ultimate deformation of the fibrous reinforced cement-based composites are all revealed in the stress-strain diagram. For further investigation, these factors are also fundamentals of the fracturing characteristics. In Fig. 2, the stress-strain curves of the cement pastes incorporated with different dosages of brucite fiber were plotted. The different amount of fibers influenced the stress-strain curves obviously. With the increasing of brucite fiber dosage, the peak compressive stress increased firstly and promptly decreased at a high fiber amount. It indicated that the incorporation of brucite fiber at a relatively low dosage increased the peak compressive through filling effect and restricting the

formation and propagation process of the micro-crack [18]. On the other hand, with relative low Young's modulus and fiber bundle dissociation ratio, brucite fibers at a high dosage cannot further improve the compressive stress. On the contrary, the deformability of fiber reinforced cement pastes increased significantly, especially at the post-peak stage under the high fiber amount, which was deemed as the quasi-ductile behavior of fiber reinforced the cement-based material. The mechanical properties under uniaxial compression were also summarized in Table S3. As reported in previous studies [13, 19-22], their results indicated that the incorporation of low elastic modulus fibers like brucite fibers in cement-based composites could decrease the elastic modulus, and increase the tensile strength and deformation ability of cement-based composite.

To Further understand the stress-strain process, the relationship between brucite fiber amount (D_{BF}) and the peak stress (δ_p) was shown in Fig. 3(a). The peak stress of the samples was increased at a low dosage before 5% compared to the control sample, and the peak stress was decreased with further increase of fiber dosage. It suggested that the peak stress of the cement paste was associated with the brucite fiber amount. The reinforcement of the brucite fiber in the cement pastes depends on its fiber bundle-splitting effect and well dispersion [1, 6]. The dispersion of the brucite fibers in the cement matrix was decreased with the increase of the brucite fiber dosage. Therefore, the agglomeration of brucite fiber at high dosage leads to the reduction of strengths of the cement composite (dosage> 5%). Such a phenomenon is also shown in Liu's work [7]. The relationship between brucite fiber and the elasticity modulus (E)

was shown in Fig. 3(b). The elasticity modulus of the cement paste was decreased with the increase of the brucite fiber dosage. Thus, the elasticity modulus of the cement pastes can be decreased significantly by incorporating brucite fibers. The relationship between the brucite fiber amount and peak displacement (d_p) was exhibited in Fig. 3(c), which showed that the peak displacement of the cement paste increased with the increase of the brucite fiber content, it has the same tendency with the development of the deformation capacity of fiber reinforced cement pastes.

3.2.2. Energy absorption capacity

In Fig. S3(a), the absorbing energy of fibrous cement-based material under uniaxial compression was determined by calculating the area of the stress-strain curve. The work of the load could be calculated by equation (1).

$$W = \int \delta d\varepsilon \quad (1)$$

Where W, δ and ε were the work by the load, load, and the displacement, respectively.

In this manuscript, the mechanical deformation capability of the cementitious material was calculated by the Chinese standard of "Steel fiber reinforced concrete testing methods (CECS13: 2009)", which was elucidated as below[14]:

The compression curve of the fiber reinforced cement paste was divided into 4 parts in Fig. S3 (b). A straight line was passed through the x-axis and the point of δ_{cra} (where δ_{cra} =0.85* δ_p), the line was also parallel to the y-axis and intersected the load curve at the critical point A. The x-coordinate of point A was the critical elastic deformation (ε_{cra}), and the area of *OAB* was defined as critical toughness of S_{OAB}.

The values of 1.2, 1.5 and 2.0 times of ε_{cra} was calculated, respectively, which were determined as the point *D*, *F*, and *H* on the load curve. The area of S_{OAB}, S_{OACD}, S_{OAEF}, and S_{OAGH} was also calculated. Hereby, the toughness indexes were defined as below:

$$\eta_{c1.0} = \frac{S_{O\sigma_p}}{S_{OAB}} \quad (2)$$

$$\eta_{c1.2} = \frac{S_{OACD}}{S_{OAB}} \quad (3)$$

$$\eta_{c1.5} = \frac{S_{OAEF}}{S_{OAB}} \quad (4)$$

$$\eta_{c2.0} = \frac{S_{OAGH}}{S_{OAB}} \quad (5)$$

The capability coefficients index was defined as below:

$$\zeta = \frac{\eta_{c,n} - a}{a - 1} \quad (6)$$

Where a was the deformation value at 1.2, 1.5 and 2.0, $\eta_{c,n}$ was the toughness index associated with the deformation value in Table S4.

The relationships between the toughness index and the dosage of the brucite fiber and the relationships between the capability coefficients index and the dosage of the brucite fiber were all presented in Fig. 3. The increasing trends of $\eta_{c1.0}$, $\eta_{c1.2}$ and $\eta_{c1.5}$ were shown in Fig. 4(a). When the brucite fiber amount was before 5%, the compressive toughness of the cement pastes increased. The growth of $\eta_{c1.5}$ was the most obvious, and the specimen of 5% was improved by 22% compared to the control sample. The increasing trend of the capability coefficients index of the cement paste was also shown in Fig. 4(b). $\zeta_{c1.2}$ and $\zeta_{c1.5}$ of 3% were 1.4 and 2.44 times than those

of the control sample, respectively. Therefore, the energy absorption capacity of the brucite fiber reinforced cementitious material can be improved at a proper fiber content.

3.3. The constitutive model of the stress-strain curve

The constitutive model of the stress-strain curve for brucite fiber reinforced cement pastes was established and analyzed to understand the deformability and loading performance of the cementitious composite. The mathematic relation which was enlightened by Zhenhai Guo et al. [23] was proposed in this part.

1. The loading curve of brucite fiber reinforced cement paste was divided into two parts (rise stage and decline stage) for fitting and elucidating as below:

$$y = a_0 + a_1 x + a_2 x^2 + a_3 x^3 \quad (x \le 1) \text{ the equation of the rise stage} \quad (7)$$

$$y = \frac{x}{b_0 + b_1 x + b_2 x^2} \quad (x \ge 1) \text{ the equation of the decline stage} \quad (8)$$

Where $x = \varepsilon / \varepsilon_p$, $y = \delta / \delta_p$ and a_0, a_1, a_2, a_3, b_0, b_1, b_2 were the calculating variate of the loading curve.

2. The rise stage ($0 \le x \le 1$)

As the loading curve showed, a_0, a_1, a_2 and a_3 should fit the geometrical feature as:

1). The curve went through the zero (x=0, y=0).

2). When $0 \le x < 1$, $\frac{\partial^2 y}{\partial x^2} < 0$, and the slope ($\frac{dy}{dx}$) of ascent curve decreased monotonically with no inflection point.

3). x=1, $\frac{dy}{dx} = 0$ and y=1 was the necessary condition of the peak point *C* on the curve.

Taking 1), 2) and 3) conditions into the equation (7), and the results were calculated as a_0=0, a_2=3-2a_1 and a_3=a_1-2. Afterward, the problem was associated with the independent variate a_1.

Then the equation (7) was turned into $y = a_1 x + (3-2a_1)x^2 + (a_1-2)x^3$ (9)

From the equation (9), when x=0, then $\frac{dy}{dx}$=a_1.

Thus, it was obtained that a_1= $\frac{dy}{dx}|_{x=0}$ = $\frac{d(\delta/\delta_p)}{d(\varepsilon/\varepsilon_p)}|_{x=0}$ = $\frac{d\delta/d\varepsilon|_{x=0}}{\delta_p/\varepsilon_p} = \frac{E_0}{E_p}$ (10)

Where $E_0 = \frac{d\delta}{d\varepsilon}|_{x=0}$ (N/mm^2) was the elasticity modulus of the initial tangent of the loading curve, and $E_p = \frac{\delta_p}{\varepsilon_p}$ (N/mm^2) was the ratio between the peak strength and peak strain as the secant modulus of the peak point on the curve. a_1 was the ratio of the initial tangent modulus to secant modulus. The decline stage of the curve was calculated by E_c and E_p. Simultaneously, the curve also should fit the condition 2), when 0≤x<1 and $\frac{\partial^2 y}{\partial x^2}$ <0, then it was obtained that:

When x=1 as $\frac{\partial^2 y}{\partial x^2}$ =2(3-2a_1) +6(a_1-2)x≤0

(x=1) → 2(3-2a_1)+6(4a_1-5)≤0

→ 20a_1≤24

→ a_1≤1.2 (11)

also the a_1= $\frac{E_0}{E_p}$ E_c>0, E_p>0,

then a_1>0 and 0<a_1≤1.2 (12)

The plots of the calculated curves at the rise stage with different values of a_1 were shown in Fig. 5(a). When a_1>1.2, the top part of the curve violated the actual test results resulted from y>1. Simultaneously, the calculated results were compared to the actual test curves in Fig. 5(b) (where the dashed lines were the calculation, and the solid lines were the test samples). When $a_1 \rightarrow 0$, the calculated curves fitted the test result well.

3. The decline stage (x≥1)

As shown in the loading curve of Fig. S5, b_0, b_1, and b_2 should fit the geometrical feature as below:

4). When x=1, $\frac{dy}{dx}=0$ and y=1 the point was the peak point *C*.

5). When $\frac{\partial^2 y}{\partial x^2}=0$, x_D>1.0, thus there was another inflection point *D*.

6). When $\frac{\partial^3 y}{\partial x^3}=0$, x_E>x_D, then the maximum curvature point of the decline stage was at point *E*.

7). When $x \rightarrow \infty$, $y \rightarrow 0$ and $\frac{dy}{dx} \rightarrow 0$, the decline stage of the curve was extended indefinitely and converged to coordinate axis. Thus, the whole curve should fit x≥0, 0<y≤1.

Taking condition 4) into the equation (8), results were obtained as b_1=1-2b_0, b_2=b_0. Therefore, b_0 was the only left parameter. Then, the equation (8) was changed to

$$y=\frac{x}{b_0(x-1)^2+x} \quad x\geq 1, \quad (13)$$

The equation (13) should fit the conditions of 5) and 6). When b_0=0, then y≡1.

As shown in the loading curve, when $b_0 \to \infty$, then $y \to 0$, after the peak point *C*, the residual stress of the cement paste approached to 0, and at this time, the cement paste was damaged completely.

Based on the condition 5), it was calculated as:

$$\frac{\partial^2 y}{\partial x^2} = \frac{2b_0[x^3 - 3x + (2 - \frac{1}{b_0})]}{[b_0(x-1)^2 + x]^3} = 0 \quad (14)$$

Afterward, the value of the point *D* was calculated (when x>1) based on the condition 6) and that was:

$$\frac{\partial^3 y}{\partial x^3} = \frac{-6b_0[b_0{}^2x^4 - 6b_0{}^2x^2 + (8b_0{}^2 - 4b_o)x - (3b_0{}^2 - 4b_0 + 1)]}{[b_0(x-1)^2 + x]^3} = 0 \quad (15)$$

Then, the maximum curvature point *E* was also calculated ($x_E > x_D$).

The decline stage of the curves against the different value of b_0 was shown in Fig. 6(a). When b_0<3, the curve of the decline stage almost was linear, and the inflection (point *D*) and maximum curvature (point *E*) were not apparent. After that, the specimen was deformed seriously. The specimen was still of a high strength which did not fit the actual test result.

The calculated curves were compared to the actual test curves in Fig. 6(b). The shape of the decline stage was complicated, and the shape was effectively impacted by the brucite fiber dosage. Fig. 6(b) showed that the decline stage had a large range of residual stress. In this manuscript, when the residual stress decreased to under 60%, the specimen of cement composite was covered with macroscopic cracks and destroyed seriously, it implied that the cement composite was a complete failure. Therefore, the range of b_0 was suggested to be 3< b_0<600.

From above, the calculated equations of the stress-strain curve depended on the brucite fiber reinforced cement paste which was under a definitive water-cement ratio. When the conditions changed, the equations should be amended as well.

4. The complete curve

To sum up, the equations of (9) and (13) were combined to represent the constitutive model of the stress-strain curves in Fig. 7(a), and the constitutive model was compared to the test curves in Fig. 7(b). The results of the experiment curves were almost contained in the calculated curves. Thus the fitted equation was valid, especially at the rise stage and the decline stage (the residual stress was over 60%). After the stress was decreased to under 60%, the cement paste was damaged completely, which had little research value in this manuscript.

Therefore, the constitutive model of the stress-strain curve of the brucite fiber reinforced cement paste was described by (12) and (16) as:

$$\begin{cases} y = a_1 x + (3-2a_1)x^2 + (a_1-2)x^3, 0 \le x \le 1 \\ y = \dfrac{x}{b_0(x-1)^2 + x}, x \ge 1 \end{cases} \quad (16)$$

Where the a_1 and b_0 were undecided parameters. And the range of a_1 and b_0 were $0<a_1\leq 1.2$ and $3<b_0<600$, respectively.

3.4. Fracture toughness analysis on brucite fiber reinforced cementitious composites

Linear elastic fracture mechanics indicated that the raw flaws and crack propagation in the cementitious material were the major causes of fracture, and the cementitious material was deemed as an isotropic material [24]. Afterward, the

previous investigation has confirmed that the cementitious composite was a heterogeneous material. Under stress, the vicinity and tip of the cracks initiated and propagated as a micro-crack area or metastable area. Thus the non-linear fracture mechanics concentrated on the fracture energy analysis of cementitious composites [24]. In this manuscript, *G* fracture criterion, double-K fracture criterion, and *J* integral were designated to quantitatively elucidate the fracture toughness of brucite fiber reinforced cementitious composite [25].

3.4.1. Methods

1. The double-K fracture model [25] was applied to determine the fracture toughness, and the fracture processes at the notch of the three-point flexural test contained three stages as crack initiation stage, crack stable growth stage and unstable failure stage. Meanwhile, the K_{Ic}^{S} was the unstable failure toughness, and the K_{Ic}^{Q} was the initiation toughness which was illustrated as below [25]:

$$K_{Ic}^{S}=\frac{1.5(F_p+\frac{mg}{2}\times10^{-2})\times10^{-3}S\sqrt{a_c}}{th^2}f(\alpha) \quad (17)$$

Where in the equation above, K_{Ic}^{S} was the unstable failure toughness (MPa·m$^{1/2}$), F_p was the peak load (kN), m was the weight on each of the welding pedestal (kg), g was the gravitational acceleration (9.81 m/s^2), S was the span of the welding pedestal (m), a_c was the critical effective crack length (m), t was the thickness of specimen (m) and h was the height of the specimen (m).

Where $f(\alpha)=\frac{1.99-\alpha(1-\alpha)(2.15-3.93\alpha+2.7\alpha^2)}{(1+2\alpha)(1-\alpha)^{3/2}}$ and $\alpha=\frac{a_c}{h}$ (18)

Besides, a_c was calculated as:

$$a_c = \frac{2}{\pi}(h+h_0)\arctan\sqrt{\frac{tEV_c}{32.6\delta_p}-0.1135}-h_0 \quad (19)$$

Where h_0 was the thickness of the steel loading plates (m), V_c was the crack mouth opening displacement (*CMOD*) (μm), and E was the elasticity modulus of the experiment curve.

Since E was calculated in (20)

$$E = \frac{1}{tc_i}[3.70+32.60\tan^2(\frac{\pi}{2}\frac{a_{c0}+h_0}{h+h_0})] \quad (20)$$

Where $c_i = \frac{\varepsilon_i}{\delta_i}$ (μm/kN), ε_i, and δ_i was any points on the loading curve, and a_{c0} was the initial notch depth (m).

The initiation toughness K_{Ic}^{Q} was defined as:

$$K_{Ic}^{Q} = \frac{1.5(\delta_Q+\frac{mg}{2}\times10^{-2})\times10^{-3}S\sqrt{a_{c0}}}{th^2}f(\alpha) \quad (21)$$

$$\text{and} \quad f(\alpha) = \frac{1.99-\alpha(1-\alpha)(2.15-3.93\alpha+2.7\alpha^2)}{(1+2\alpha)(1-\alpha)^{3/2}}, \quad \alpha = \frac{a_{c0}}{h} \quad (22)$$

Where K_{Ic}^{Q} was the initiation toughness (MPa·m$^{1/2}$), δ_Q was initiate load (kN) which was the load of the inflection point at the ascending stage.

2. The fracture energy (G_F) [26] of the specimen was calculated according to RILEM TC-50 FMC. The G_F was calculated from the area covered underneath the midspan of loading-deflection curves [27, 28]. And during the three-point flexural test, the actual work of external force was consisted by three parts: the work by an external force on the test specimen (W_0), work of the specimen weight between the welding pedestals (m_1g) and work of the loading device weight (m_2g) on the specimen. Thus, the external force P was:

$$P = \frac{1}{2} m_1 g + m_2 g \quad (23)$$

Moreover, the energy of fracture experiment was plotted in Fig. S4 and the work of the resultant force was: $Wz = W_0 + W_1 + W_2 + W_3$ (24)

Where the *Wz* was the work of resultant force, W_0 was the work of external force, W_1, W_2, and W_3 were the work of weight by the test system. Thereinto, the W_3 can be ignored and $W_1 \approx W_2$, thus:

$$W_z = W_0 + 2W_1 \quad (25)$$

$$W_1 = (\frac{1}{2} m_1 g + m_2 g)\lambda_{max} \quad (26)$$

Where the λ_{max} was the maximum of the deflection (m).

From above, the fracture energy was calculated as:

$$G_F = \frac{Wz}{A_{lig}} = \frac{W_0 + W_g}{A_{lig}} = \frac{W_0 + mg\lambda_{max}}{A_{lig}} \quad (27)$$

Where the G_F (N/m) was the fracture energy, W_0 (N·m) was the area of the load-deflection curve, $m=1/2m_1+m_2$ (kg), A_{lig} (m^2) was the area of the toughness notch:

$$A_{lig}=t(h-a_{c0}) \quad (28)$$

3. *J* integral was employed on the energy analysis which is a measure of fracture criterion for fiber–reinforced concrete, the following equation [29,30]:

$$J = \frac{2U}{t(h-a_{c0})} \quad (29)$$

$$U = \int_0^{\lambda} P d\lambda \quad (30)$$

Where λ (m) was the deflection and *U* (J) was the deflection work. From equation (30), the maximum load was employed to determinate the critical value (J_c).

3.4.2. Fracture toughness and energy

The fracture toughness parameters were analyzed and presented in Table S5 based on the load-deflection curves of the three-point bending test. The obtained results showed that both K_{Ic}^{S} and K_{Ic}^{Q} were increased with the increase of the brucite fiber dosage as shown in Fig. 8. Furthermore, the rate of increase (K_{Ic}^{S}) were 27.7%, 107.4%, 148.4%, 450.6%, 209.7% and 222.3% at 1%, 3%, 5%, 8%, 10% and 12% of the brucite fiber amount, respectively. The rate of growth (K_{Ic}^{Q}) were 26.5%, 63.5%, 67.5%, 98.5%, 86.2% and 91.8% at the brucite fiber amount of 1%, 3%, 5%, 8%, 10% and 12%, respectively. Apparently, the fracture toughness of both parameters was increased up to 8% amount (the optimum dosage). Whereas a decline occurred thereafter, it has the same tendency of with the tensile strength results. The relationship between peak load and brucite fiber dosage, and the relationship between K_{Ic}^{S} and tensile strength were presented in Fig. 9(a-b). It indicated that the fracture toughness of cement pastes was significantly influenced by the samples' strength, especially the tensile strength. Besides, the sample with higher tensile strength also exhibited a higher fracture toughness.

The fracture toughness energy (G_F) and J-integral (J_c) of brucite fiber reinforced cementitious composites were presented in Table S6, respectively. The results showed that G_F and J_c increased with the enhancement of the brucite fiber amount Fig. 10(a-b). For linear elastic fracture toughness, the increase rates of G_F were -7.3%, 93.3%, 454.9%, 378.8%, 262.7% and 252.5% at the brucite fiber amount of 1%, 3%, 5%, 8%, 10% and 12%, respectively. The optimum dosage for best linear elastic fracture

toughness energy (G_F) was 5% amount. For the elastic-plastic fracture toughness parameter J_c, the rates of J_c were -24.9%, 50.9%, 279.2%, 212.9%, 96.7% and 90.7% at the brucite fiber amount of 1%, 3%, 5%, 8%, 10% and 12%, respectively. The increase in the amount of the brucite fiber exhibited a significant increase and enhancement of cementitious composite fracture toughness energy. Furthermore, the optimum dosage for maximum J_c was also 5%, and the reduction was found at 1%, it was deduced that at a relatively low content, the incorporation of brucite fiber did not effectively enhance the fracture toughness energy. Both the parameters of G_F and J_C are calculated to elaborate the toughness capacity of the cement-based composite incorporating brucite fiber. Due to the brucite fiber possesses high specific surface area, intrinsic fibrous anisotropy, and network topology, the brucite fiber reinforced cement exhibit advantages of greater bending strength and crack bridging, as well as better crack resistance properties.

3.5. Microstructure

The microstructure of the brucite fiber reinforced cement paste surface was observed *via SEM* as presented in Fig. 11. Brucite fiber was curl and clumping, and under high magnification, it consisted of fiber bundles. As reported by Guan et al. [10], the brucite fiber is produced in bundles, and the fiber bundles are formed by a number of single fibers, which have diameters in the nanometer level. According to the previous studies [31-35] the dispersed single brucite fiber has an aspect ratio (exceeding 100), and the diameter of brucite fiber bundle is approximate 1.5-16.3μm, the dispersed single fiber is around 45-110nm in diameter. Thus, there are about

15-363 fibers in a bundle. When the brucite fiber was pre-dispersed and mixed with the cement powders, the fiber bundle was disassembled into numbers of slender and short fibers (Fig. 11(c)). Therefore, the performance of the brucite fibrous cement composite was severely influenced by the distribution of the brucite fiber.

The SEM observation exhibited that brucite fibers at a reasonable dosage can distribute well in the cement matrix without fiber clumping or fiber balling (Fig. 11(d)). Furthermore, enormous distributed short brucite fibers were embedded into the cement matrix and formed a multi-size fibrous net structure that was indicated by the filling effect (Fig. 11(e-f)). Besides, the short brucite fiber was observed bridging over the cracks (Fig. 11(e)), which restricted the crack propagation. Therefore, the fiber failure mechanisms of the brucite fiber were fiber breakage and fiber bridging. Due to the brucite fiber was well-bonded with the cement paste for surface hydrophilic and the moderate strength. The fracture toughness and mechanical performance of the fibrous cementitious composite were enhanced effectively by incorporating the brucite fiber.

4. Conclusion

1. The incorporation of brucite fiber in the cement-based composite limits the reinforcement of the compressive strength, but it displays an improvement effect on the tensile strength and deformability.

2. The deformability of fiber reinforced cement pastes increases significantly, and the mathematical fitting relationships between brucite fiber content and the peak stress, elasticity modulus as well as peak strain are exhibited, respectively.

3. The constitutive model of the stress-strain curve of the brucite fiber reinforced cement paste is described as:

$$\begin{cases} y = a_1 x + (3-2a_1)x^2 + (a_1-2)x^3, 0 \le x \le 1 \\ y = \dfrac{x}{b_0(x-1)^2 + x}, x \ge 1 \end{cases} \quad (16)$$

4. The brucite fibers can increase the fracture toughness (K_{Ic}) of the cementitious composite, and the fracture toughness is significantly influenced by the matrix strength, especially the tensile strength.

5. Due to the brucite fiber possesses a intrinsic fibrous anisotropy, and network topology, the brucite fiber reinforced cement exhibit advantages of greater bending strength, crack bridging and better crack resistance property.

Acknowledgments

This work was jointly supported by the financial support by Sichuan Science and Technology Program (2017FZ0046, 2018JZ0026), China Postdoctoral Science Foundation (2017M610600), the Fundamental Research Funds for the Central Universities (Full-time Postdoctoral Research Fund of Sichuan University, 2017SCU12016), Hong Kong Scholars Program. We would like to thank Wang Hui (Analytical & Testing Center, Sichuan University) for her help in SEM observation, respectively.

Reference

1. B., Guan, S., Chen and K., Liu. Mechanical poperty of brucite fiber reinforced composite material. Applied Mechanics & Materials. 2013, 357-360, 1019-1022.

2. F., Dong, P., Wan, Z., Pan, K., Zhou, T., Peng. Study on applied mineralogy of fibrous brucite(FB), 1st edition. Sichuan Science and Technology Press, Chengdu, 1997, Chapter 4 section 3, 117.

3. F., Dong, J., Liu and S., Luo. Environmental safety investigation on fibrous brucite. Bulletin of Mineralogy Petrology & Geochemistry. 1997, 16, 43-46.

4. J., Deng, Y., Wu, S., Zhao, Y., Song and F., Dong. Effects of acid treated fibrous brucite on hemolytic activities. Industrial Health & Occupational Diseases. 2000, 26, 76-77.

5. R., Zheng and K., Wei. Utilization and development of the brucite resources in China. China Mines Industry. 1998, 7, 21-23.

6. Z.,Wang, P., Yu and S., Lu. Study of pre-dispersive technology of brucite fiber and the composite insulation board. Materials Science Forum. 2016, 852, 1010.

7. K., Liu, H., Cheng and J., Zhou. Investigation of brucite-fiber-reinforced concrete. Cement & Concrete Research. 2004, 34, 1981-1986.

8. B., Guan, S., Chen and K., Liu. Mechanical property of brucite fiber reinforced composite material. Applied Mechanics & Materials. 2013, 357-360, 1019-1022.

9. X., Rui, B., Guan and Y., Sheng. Anti-fatigue property of brucite fiber reinforced asphalt mixture under sulfate and dry-wet circle corrosion environment. Journal of Wuhan University of Technology. 2014, 10, 45-51.

10. B., Guan, R., Xiong, R., He, S., Chen and D., Ding. Investigation of usability of brucite fiber in asphalt mixture. International Journal of Pavement Research & Technology. 2014, 7, 193-202.

11. B., Guan, S., Chen and R., Xiong. Low temperature anti-cracking performance of brucite-fiber-reinforced asphalt concrete. Advanced Materials Research. 2011. 228-229, 23-28.

12. X., Li and J., Zhuang. Performance research of brucite fibers reinforced oil well cement paste. Oilfield Chemistry. 2015, 32, 169-174 and 184.

13. M., Li, Y., Yang, J., Jin, Y., Yu and X., Guo. Reinforced mechanical properties and mechanism of well-cementing stones by brucite fiber. Natural Gas Industry. 2015, 6, 1-5.

14. Y., Yang, S., Fu and X., Li. Mechanical attributes of uniaxial compression for calcium carbonate whisker reinforced oil well cement pastes. Advances in Materials Science and Engineering. 2017, 4, 1-13.

15. S., Xu and Y., Zhu. Experimental determination of fracture parameters for crack propagation in hardening cement paste and mortar. International Journal of Fracture. 2009, 157, 33-43.

16. S., Park, J., Dong and G., Ryu and K., Koh. Tensile behavior of ultra high performance hybrid fiber reinforced concrete. Cement & Concrete Composites. 2012, 34, 172-184.

17. H., Pakravan, M., Latifi and M., Jamshidi. Hybrid short fiber reinforcement system in concrete: A review. Construction & Building Materials. 2017, 142, 280-294.

18. Z., Wang and P., Xin. Experimental study on the uniaxial compression properties and the stress-strain curves of UHS & HPC. Journal of Chongqing Jianzhu University. 2000, 22, 27-33.

19. Y., Yang, and Y., Deng. Mechanical properties of hybrid short fibers reinforced oil well cement by polyester fiber and calcium carbonate whisker. Construction and Building Materials. 2018, 182, 258-272.

20. Z., Liu, Z., Bian, C., Liu, X., Zhou and S., Dai. Experimental study of influence of polyester fibre on shrinkage cracks of cement-stabilized macadam. Journal of China University of Mining & Technology. 2009, 38, 155-158.

21. N., Jafariesfad, M., Geiker, Y., Gong, P., Skalle, Z., Zhang and J., He. Cement sheath modification using nanomaterials for long-term zonal isolation of oil wells: Review. Journal of Petroleum Science & Engineering. 2017, 156, 662-672.

22. T., Trapko. Behaviour of fibre reinforced cementious matrix strengthened concrete columns under eccentric compression loading. Materials & Design. 2014, 54, 947-954.

23. Z., Guo. The strength of the concrete and constitutive relation. Beijing, China: Architecture & Building Press. 2004, 1 ed., 50-102.

24. N., Perez. Linear-elastic fracture mechanics. Springer International Publishing. 2017, 64-76.

25. S., Xu. Concrete fracture test and fracture toughness measurement standard method. Beijing, China: Machine Press. 2010, 1 ed, 16-23.

26. J., Manning, C., Lee, A., Cerami and P., Gillette. Draft recommendation: Determination of the fracture energy of mortar and concrete by means of three-point bend tests on notched beams. Materials & Structures. 1985, 18,484-484.

27. A., Noaman, B., Bakar and H., Akil. Experimental investigation on compression toughness of rubberized steel fibre concrete. Construction & Building Materials. 2016, 115, 163-170.

28. E., Güneyisi, M., Gesoglu, T., Özturan and S., İpek. Fracture behavior and mechanical properties of concrete with artificial lightweight aggregate and steel fiber. Construction and Building Materials. 2015, 84, 156-168.

29. K., Mo, K., Yap, U., Alengaram and M., Jumaat. The effect of steel fibres on the enhancement of flexural and compressive toughness and fracture characteristics of oil palm shell concrete. Construction and Building Materials. 2014, 55, 20-28.

30. A., Noaman, B., Bakar, H., Akil and A., Alani. Fracture characteristics of plain and steel fibre reinforced rubberized concrete. Construction & Building Materials. 2017, 152, 414-423.

31. X., Cao, X., Chuan, S., Zhou and H., Huang. Surface modification of natural fibrous brucite with stearic acid. Journal of Wuhan University of Technology (Material Science). 2016, 31, 108-112.

32. F., Dong, B., Zhang, W., Wang, G., Wang and K., Zheng. Studies on past-processing and antibacterial properties of natural fibrous brucite. Journal of Functional Materials. 2010, 41, 862-865.

33. L., Xu, W., Ni, W., Li. Preparation of Natural brucite nanofibers by the dispersion method. Journal of University of Science and Technology. 2008, 15, 489-494.

34. F., Dong, Z., Pan, P., Wan. Studies on the application mineralogy of fibrous brucite in heimulin of southern shaanxi province. Earth Sciences. 1993, 5, 642.

35. Z., Sun and K., Liu. Dispersion of brucite fiber and its application in concrete. China Concrete and Cement Products. 2010, 2, 50-52.

Captions of figures and tables

Fig. 1. (a) The strength properties of type A brucite reinforced cement pastes, and (b) the strength properties of type B brucite reinforced cement pastes.

Fig. 2. The stress-strain curve of brucite fiber reinforced cement pastes.

Fig. 3. Fig. 3. (a) Plot of peak stress with DBF for cement-based materials with brucite fiber, (b) plot of elasticity modulus with DBF for cement-based materials with brucite fiber, (c) plot of peak strain with DBF for cement-based materials with brucite fiber.

Fig. 4. (a) The toughness index of brucite fiber reinforced cement paste, and (b) the capability coefficients index of brucite fiber reinforced cement paste.

Fig. 5. (a) a_1 and the calculated curve at the ascent stage, and (b) the calculated curve contrast to the test curve.

Fig. 6. (a) b_0 and the calculated curve at the descent stage, and (b) calculated curve compared to the test curve.

Fig. 7. (a) The calculated curve of the constitutive model, and (b) the integrated calculated curve compared to the complete test curve.

Fig. 8. (a) The relationship between K_{Ic}^{S} and brucite fiber dosage, and (b) the relationship between K_{Ic}^{Q} and brucite fiber dosage.

Fig. 9. (a) The relationship between peak load and brucite fiber dosage, and (b) the relationship between K_{Ic}^{S} and tensile strength.

Fig. 10. (a) The relationship between G_F and brucite fiber dosage, and (b) the relationship between J_c and brucite fiber dosage.

Fig. 11. *SEM* micrographs of brucite fibers before and after incorporation: (a) brucite fibers before incorporation, (b) high magnification of the brucite fiber, (c) dispersion of the brucite fiber, (d) brucite fibers distributed well in the cement matrix, (e) bridging effect of the brucite fiber, (f) short brucite fibers embedded into the cement.

Table 1. The proportion of cement and fibrous cement slurry.

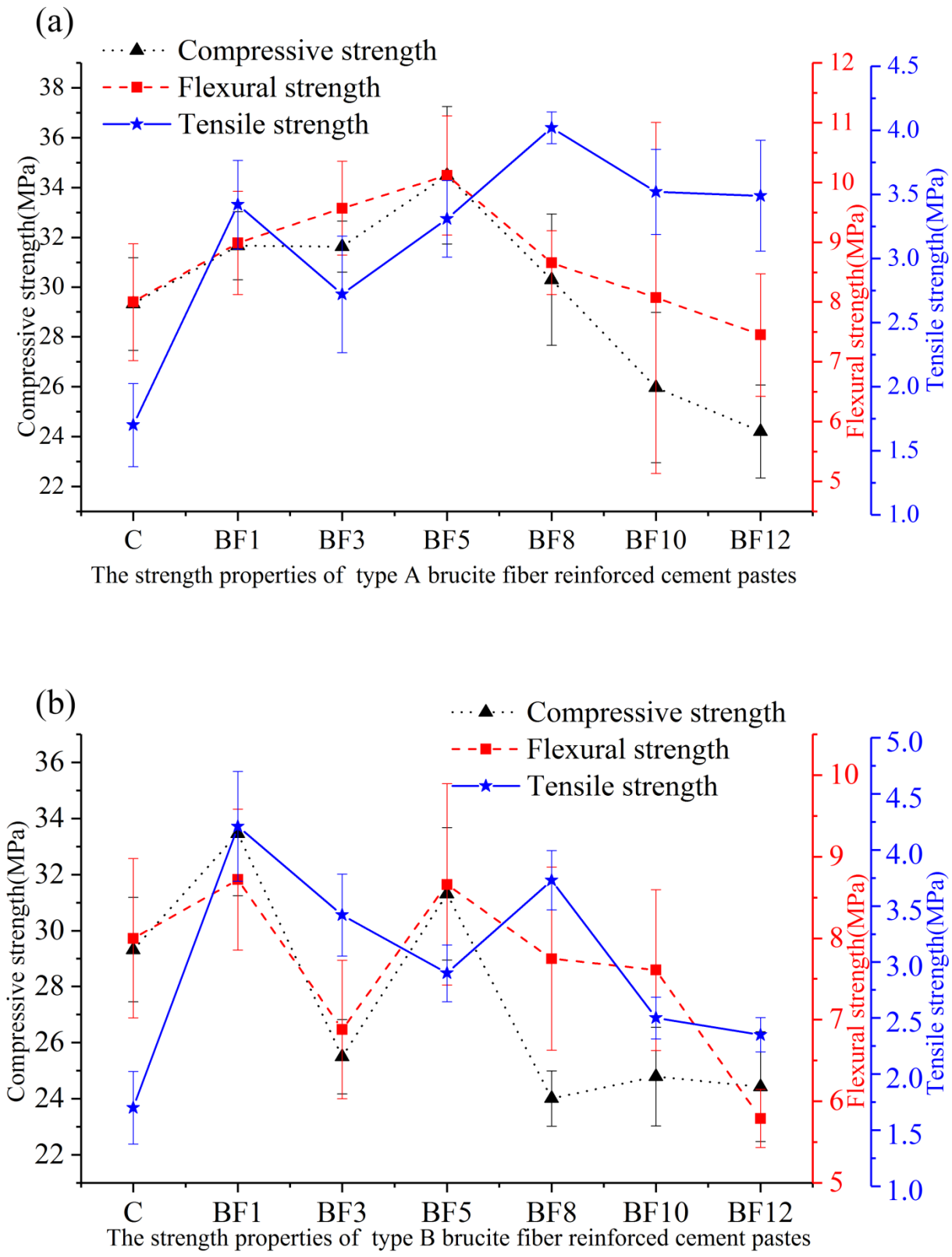

Fig. 1. (a) The strength properties of type *A* brucite reinforced cement pastes, and (b) the strength properties of type *B* brucite reinforced cement pastes.

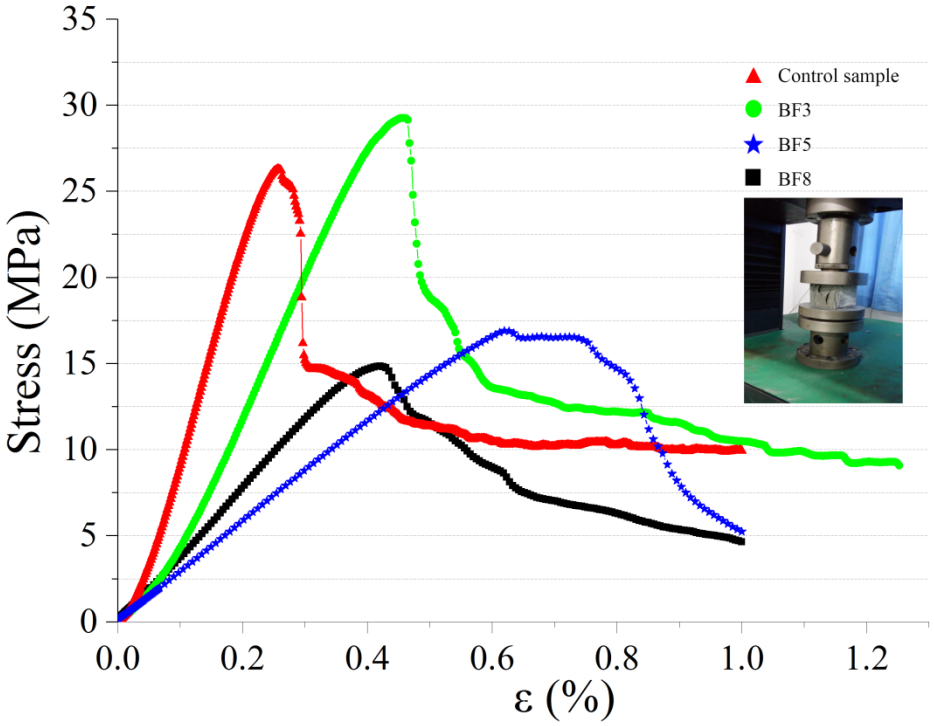

Fig. 2. The stress-strain curve of brucite fiber reinforced cement pastes.

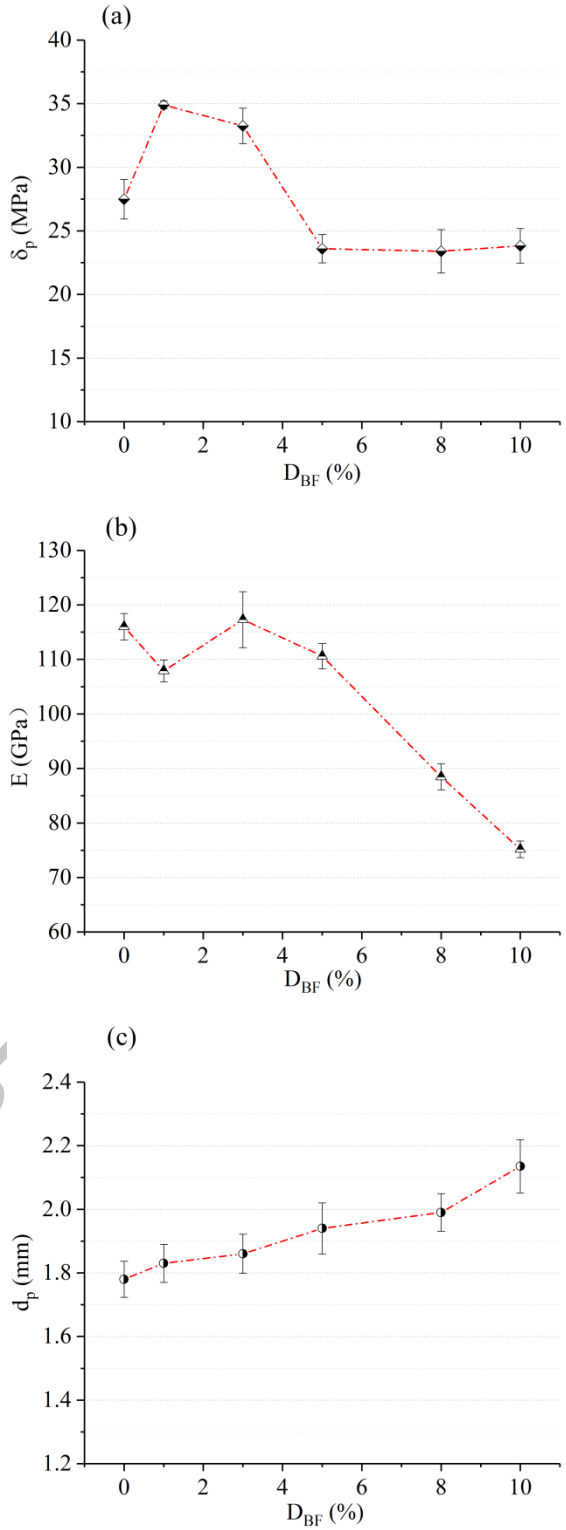

Fig. 3. (a) Plot of peak stress with D_{BF} for cement-based materials with brucite fiber, (b) plot of elasticity modulus with D_{BF} for cement-based materials with brucite fiber, (c) plot of peak strain with D_{BF} for cement-based materials with brucite fiber.

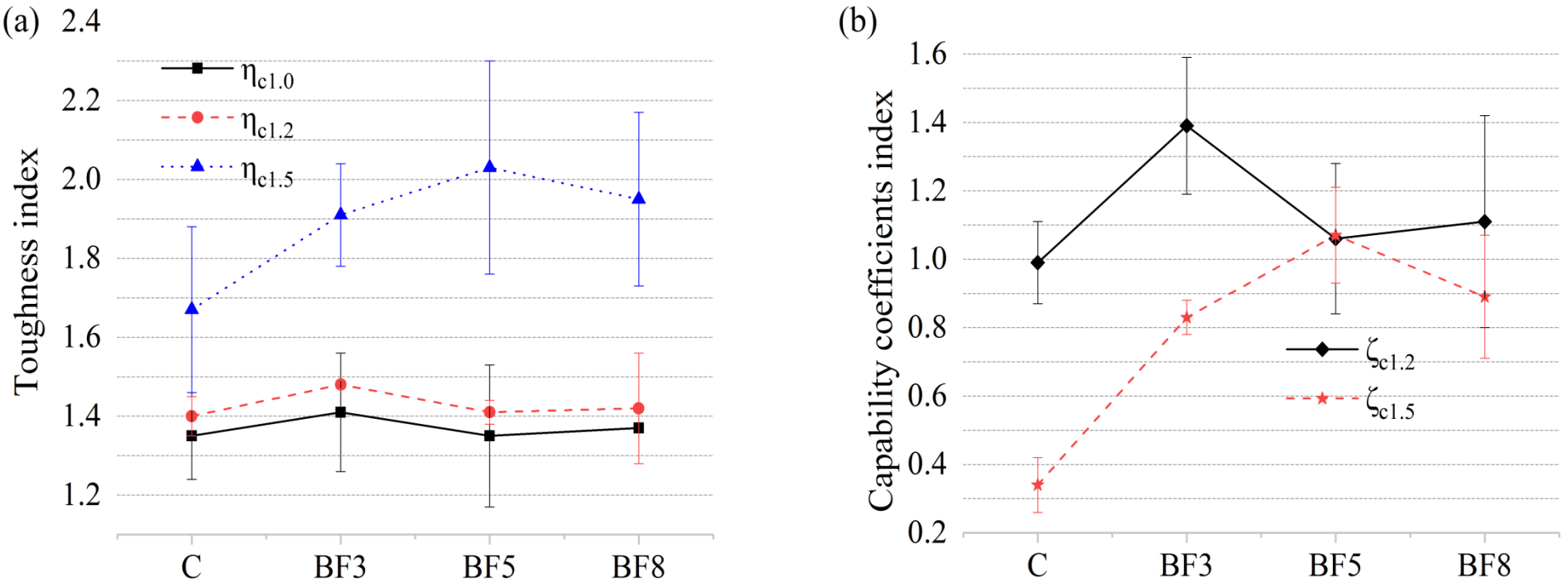

Fig. 4. (a) The toughness index of brucite fiber reinforced cement paste, and (b) the capability coefficients index of brucite fiber reinforced cement paste.

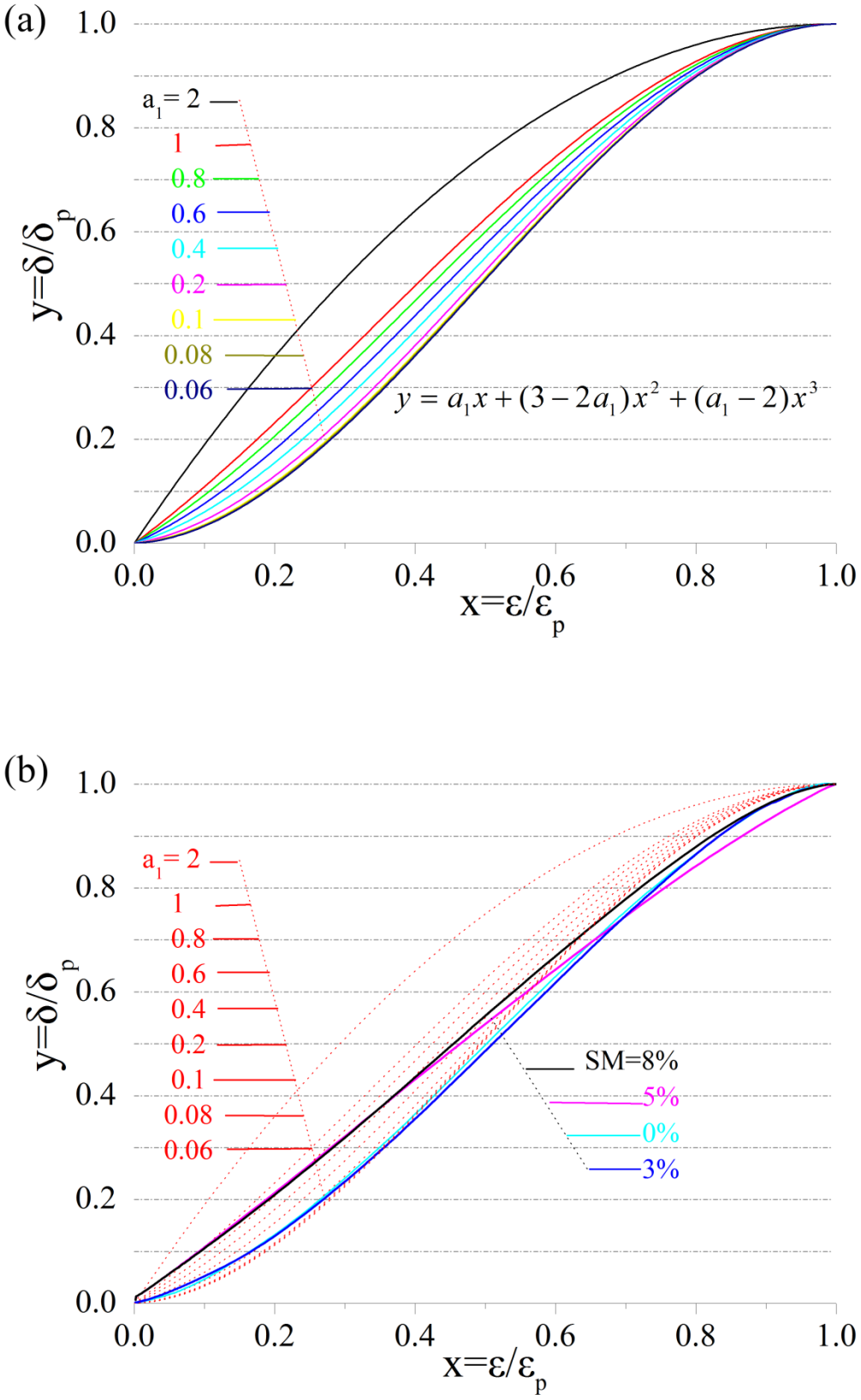

Fig. 5. (a) a_1 and the calculated curve at the ascent stage, and (b) the calculated curve contrast to the test curve.

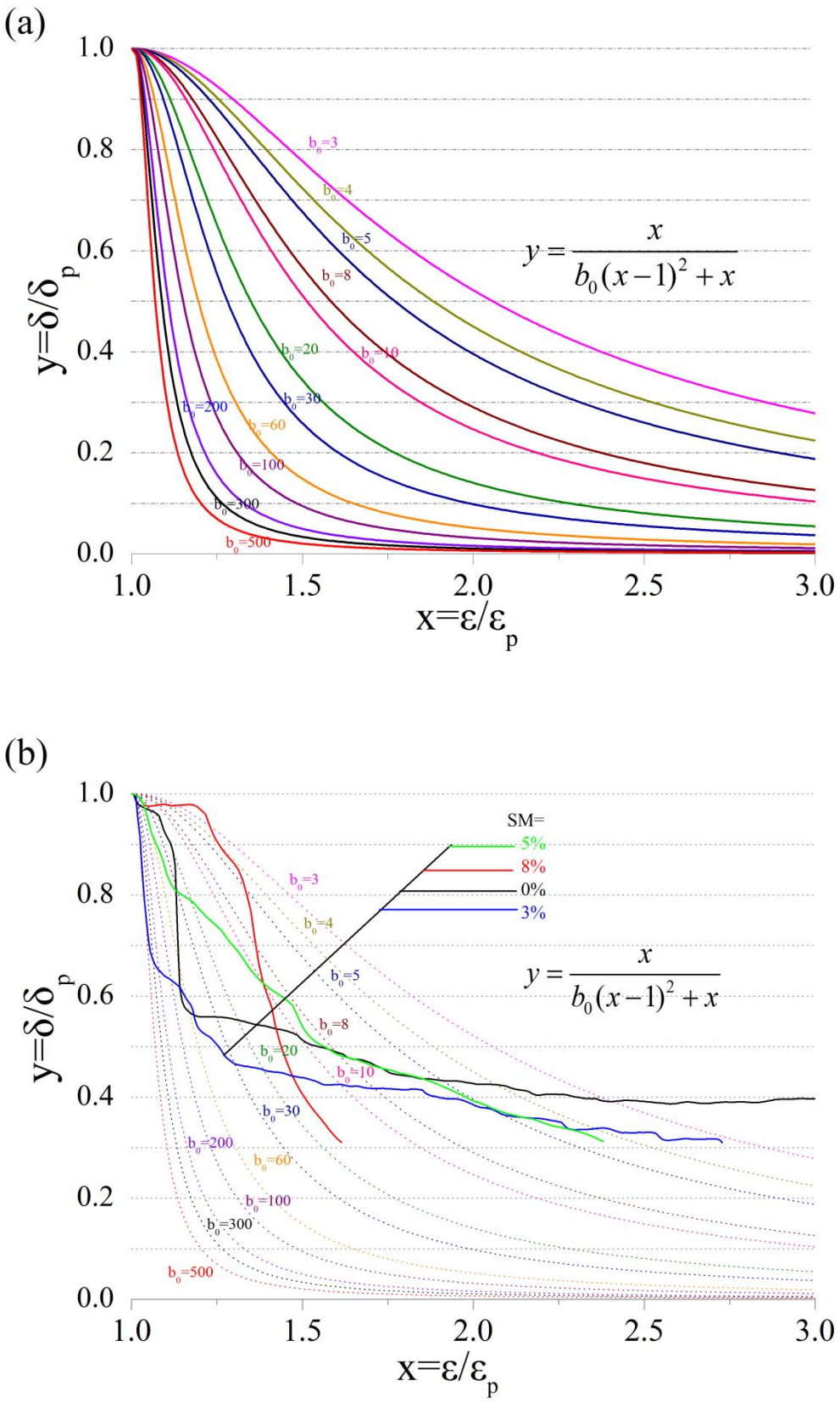

Fig. 6. (a) b_0 and the calculated curve at the descent stage, and (b) calculated curve compared to the test curve.

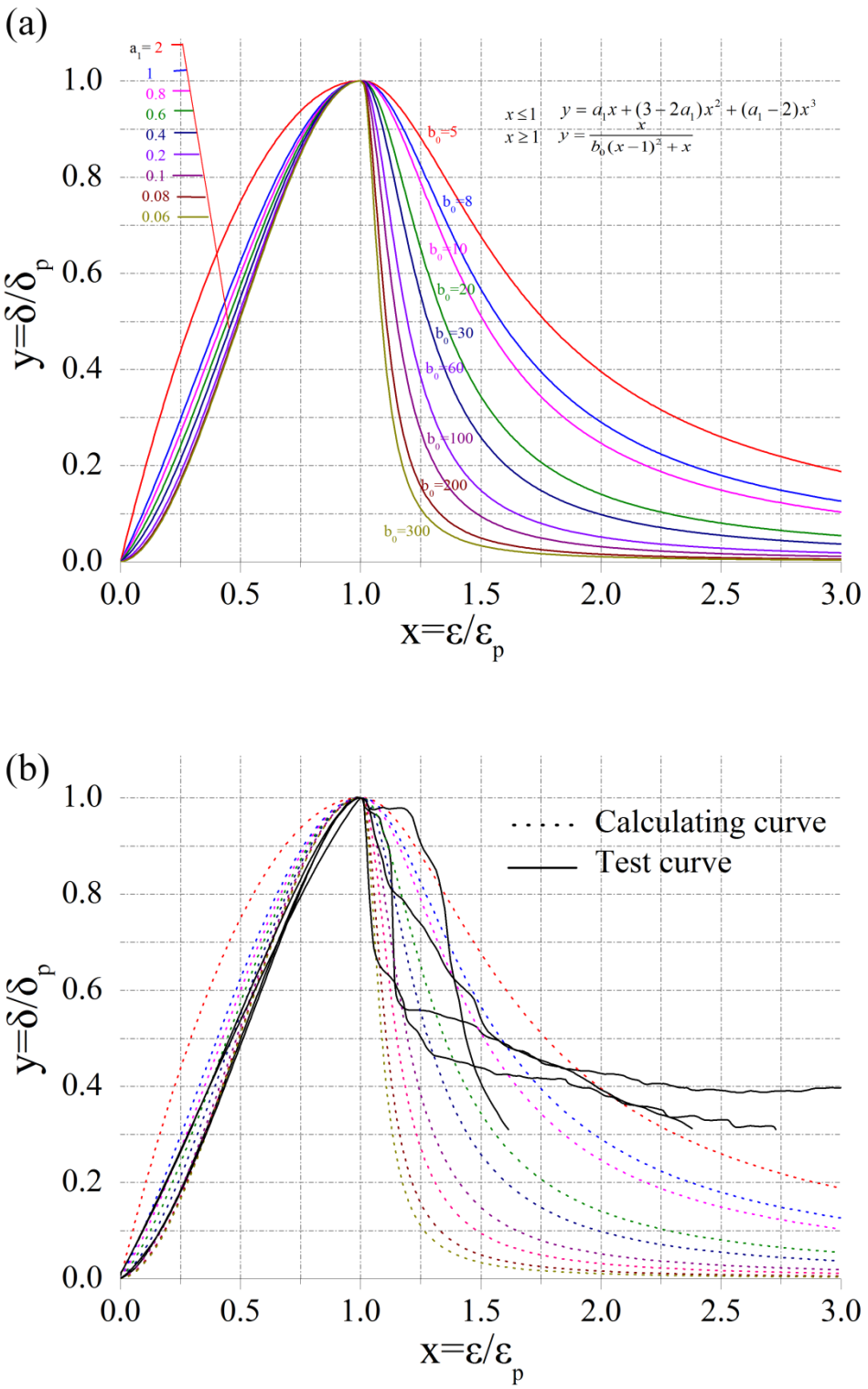

Fig. 7. (a) The calculated curve of the constitutive model, and (b) the integrated calculated curve compared to the complete test curve.

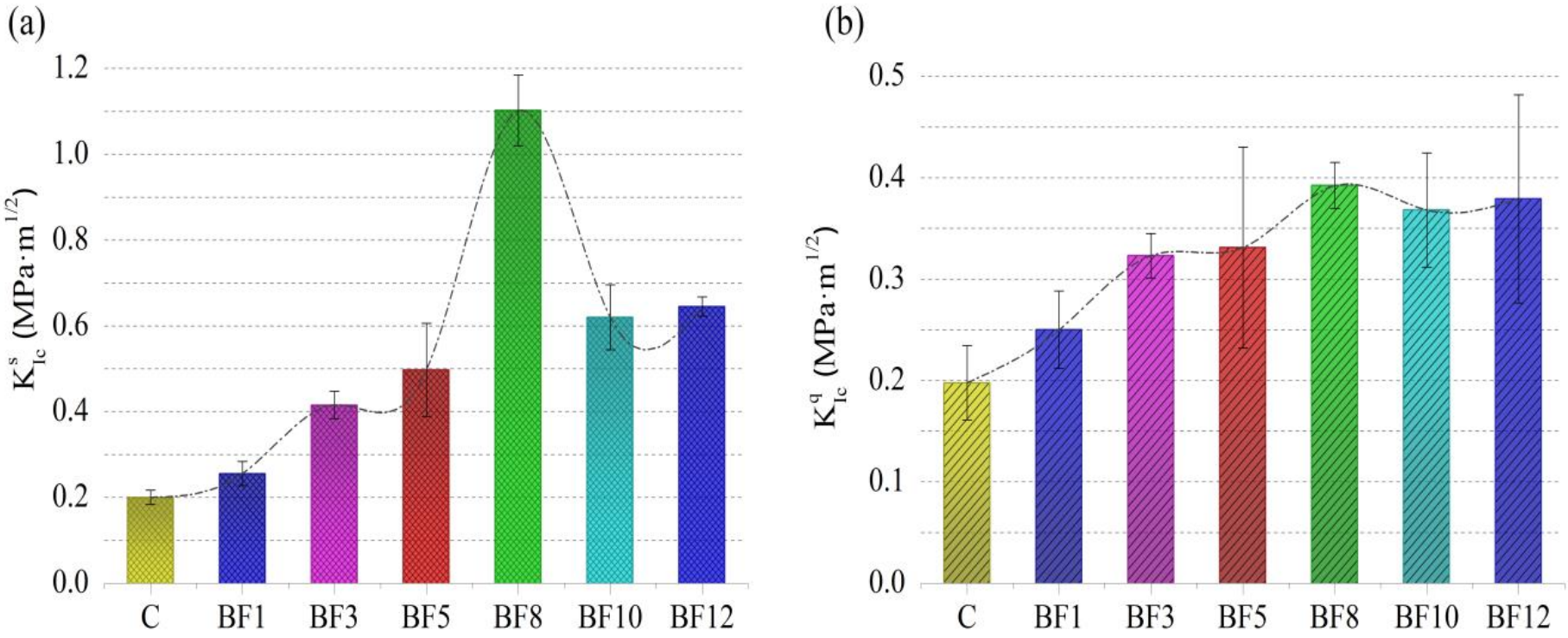

Fig. 8. (a) The relationship between K_{Ic}^{S} and brucite fiber dosage, and (b) the relationship between K_{Ic}^{Q} and brucite fiber dosage.

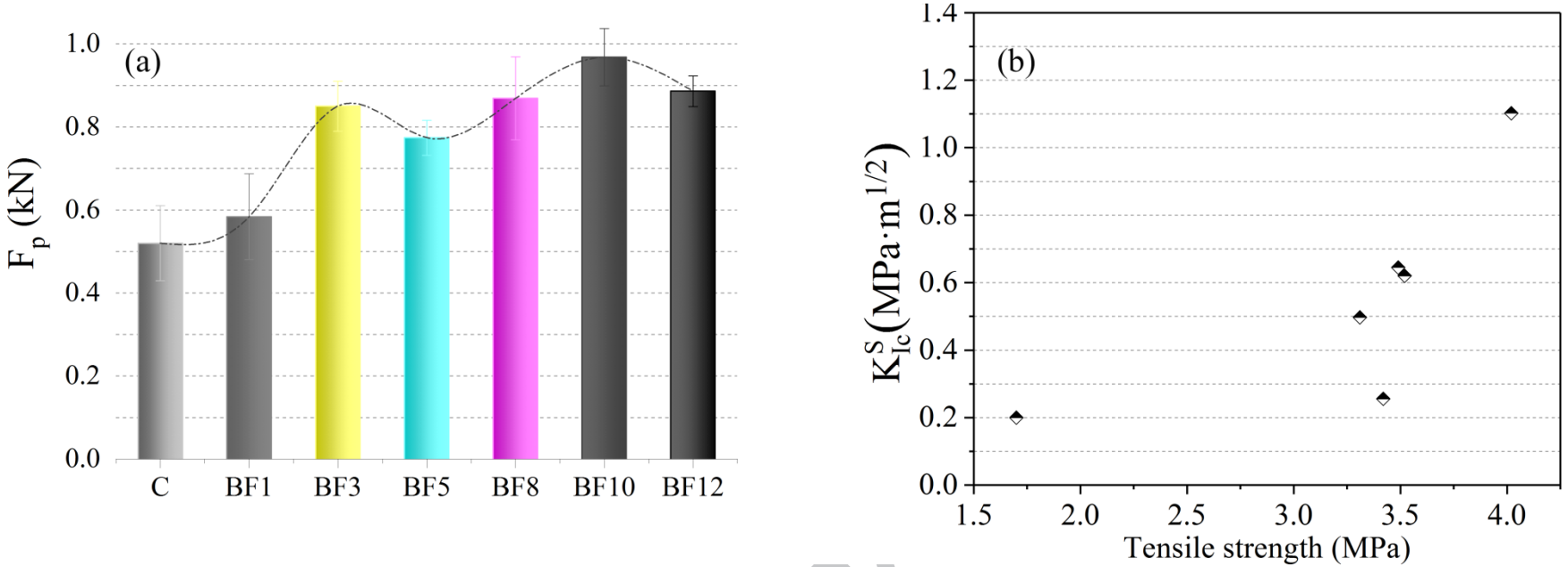

Fig. 9. (a) The relationship between peak load and brucite fiber dosage, and (b) the relationship between K_{Ic}^S and tensile strength.

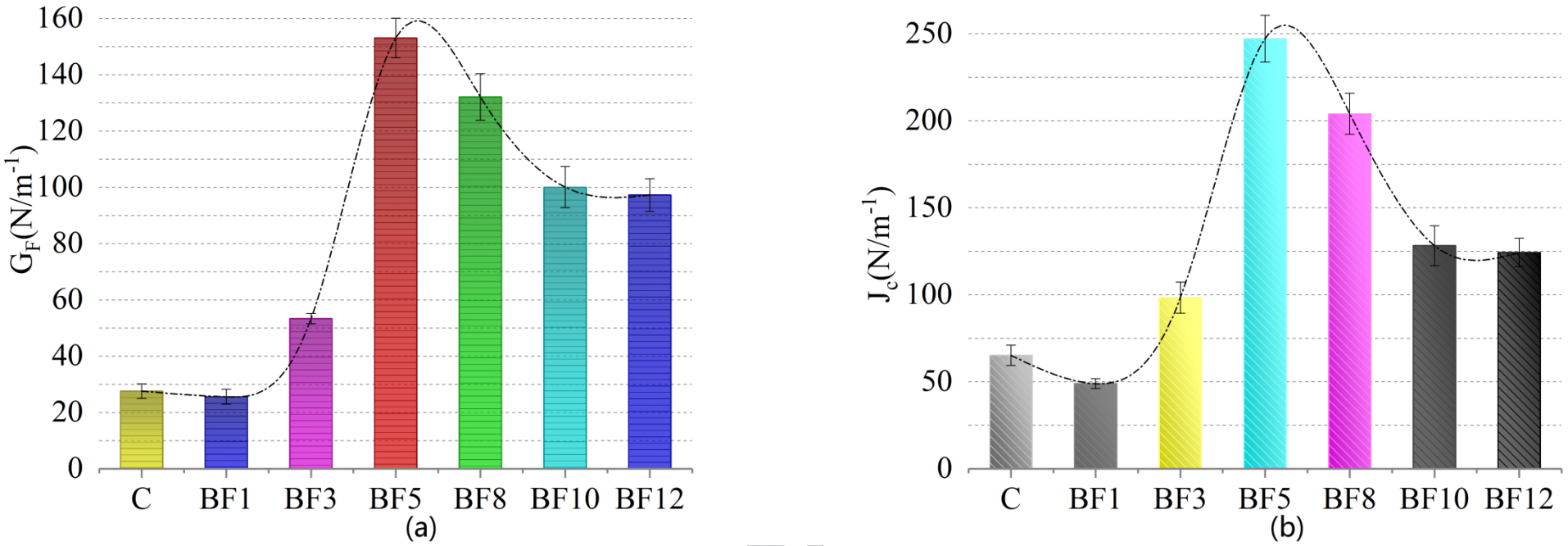

Fig. 10. (a) The relationship between G_F and brucite fiber dosage, and (b) the relationship between J_c and brucite fiber dosage.

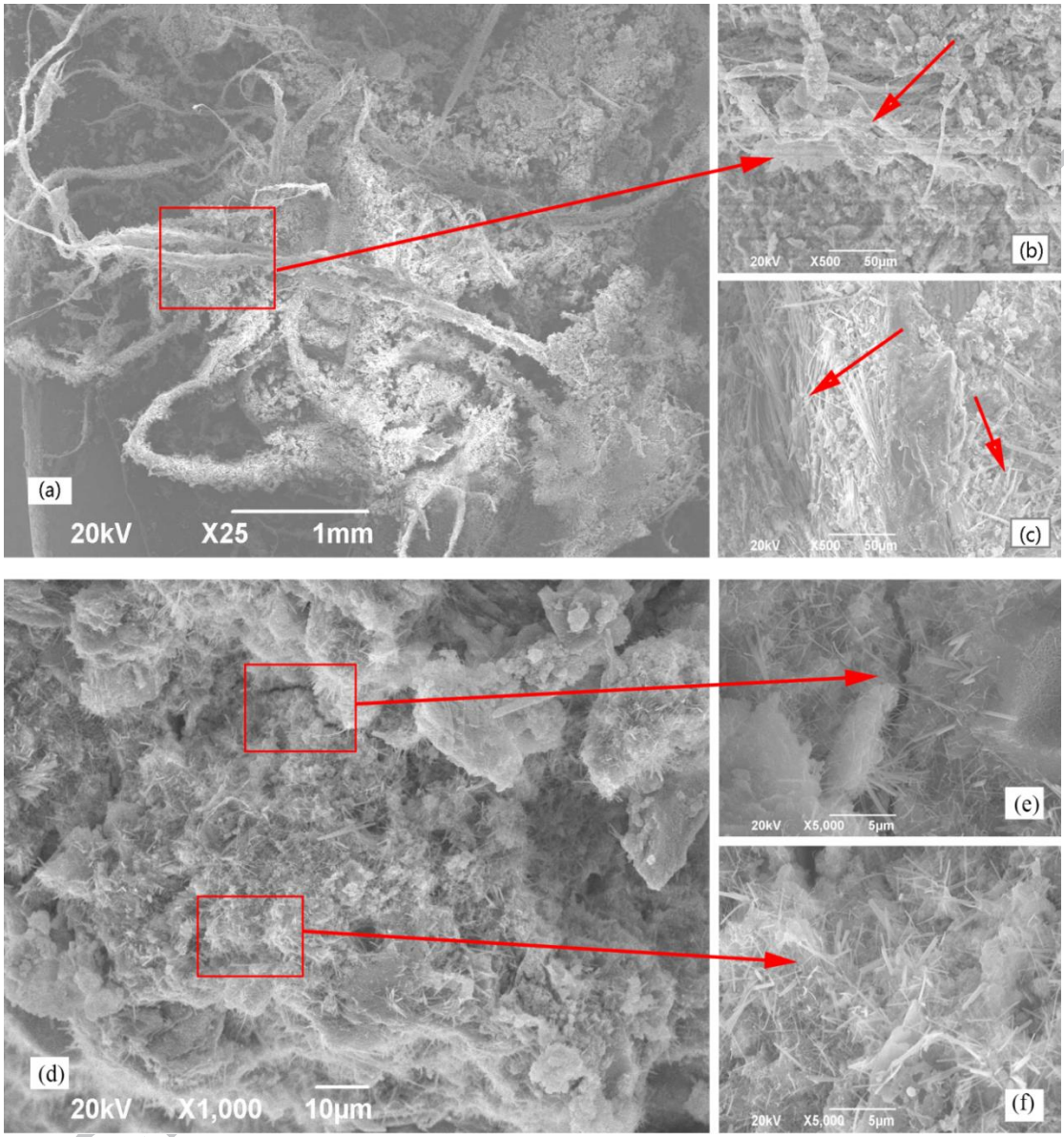

Fig. 11. SEM micrographs of brucite fibers before and after incorporation: (a) brucite fibers before incorporation, (b) high magnification of the brucite fiber, (c) dispersion of the brucite fiber, (d) brucite fibers distributed well in the cement matrix, (e) bridging effect of the brucite fiber, (f) short brucite fibers embedded into the cement.

Table 1. The proportion of cement and fibrous cement slurry.

Sample	Cement (g)	Filtrate reducer (g)	Superplasticizer (g)	Water (g)	Brucite fiber (g)	W/B
C	1600	32	8	704	0	0.44
BF1	1584	20	24	704	16	0.44
BF3	1552	20	24	704	48	0.44
BF5	1520	20	24	704	80	0.44
BF8	1472	20	24	704	128	0.44
BF10	1440	20	24	704	160	0.44
BF12	1408	20	24	704	192	0.44